H. Examples of numerical simulations

This chapter presents examples of numerical simulation. All simulations are conducted using the fully compressible version of the nonhydrostatic model with the HI-VI scheme (e.g., "MRI-NHM").

H-1. Basic verification against 3-D linear mountain waves[1]

Ikawa and Saito (1991) verified the model-simulated mountain flow over a three-dimensional mountain. However, at that time, the anelastic-scheme with the Boussinesq approximation was used for the model. In this chapter, we show the basic verification once again to demonstrate the model's progress after publication of Ikawa and Saito (1991). The design of verification is almost the same as in Ikawa and Saito (1991), but the fully compressible version is employed and the amplification effect of the mountain waves due to decrease of the density of the reference atmosphere is considered both in the numerical simulation and the analytic solution.

H-1-1 Linear analytic solution of 3-D mountain waves

For steady state, stratified Boussinesq fluid, the vertical displacement of streamlines $\delta(x, y, z)$ of linear mountain waves is given as

$$\frac{\partial^2}{\partial x^2}\left(\frac{\partial^2}{\partial x^2}+\frac{\partial^2}{\partial y^2}+\frac{\partial^2}{\partial z^2}\right)\delta+\frac{N^2}{U^2}\left(\frac{\partial^2}{\partial x^2}+\frac{\partial^2}{\partial y^2}\right)\delta=0, \tag{H1-1-1}$$

where U is the environmental wind speed and N, the Brunt-Vaisala frequency:

$$N^2=\frac{g}{\bar{\theta}}\frac{d\bar{\theta}}{dz}. \tag{H1-1-2}$$

Here, θ is the potential temperature of the environmental atmosphere.

With constant N and U, the solution of (H1-1-1) is obtained by using double-Fourier transform analysis (Smith, 1980):

$$\delta(x,y,z)=\iint_{-\infty}^{\infty}H(k,l)\,e^{imz}e^{i(kx+ly)}dkdl, \tag{H1-1-3}$$

where $H(k,l)$ is the double-Fourier transform of the orography height $h(x,y)$ defined as

$$H(k,l)=\frac{1}{4\pi^2}\iint_{-\infty}^{\infty}h(x,y)\,e^{-i(kx+ly)}dxdy. \tag{H1-1-4}$$

Here, m in (H1-1-3) is calculated by the horizontal wave number vector (k,l) as

$$m^2=\frac{k^2+l^2}{k^2}\left(\frac{N^2}{U^2}-k^2\right). \tag{H1-1-5}$$

For the upper radiation condition, the positive imaginary root of (H1-1-5) is chosen for $k^2>N^2/U^2$, while the sign of m is chosen to be the same as that of k for $k^2<N^2/U^2$. Once δ is obtained, the vertical wind component w is given by the following linear relation for steady flow:

$$w=U\frac{\partial\delta}{\partial x}. \tag{H1-1-6}$$

In this study, in order to express the amplification effect of the mountain waves due to the decrease of density of the reference atmosphere ρ, we multiply the amplitude of the w-field by the following amplification

[1]Part of this section was extracted from the results reported in Saito *et al.* (1998).

factor:

$$\left(\frac{\bar{\rho}}{\bar{\rho}_0}\right)^{-\frac{1}{2}}=\left[e^{-Sz}\left\{1-\frac{g}{c_p\theta_o S}(1-e^{-Sz})\right\}^{\frac{c_p}{R}}\right]^{-\frac{1}{2}}. \qquad \text{(H1-1-7)}$$

Here, S is the static stability ($=N^2/g$), g the gravity acceleration, c_p the specific heat of air at constant pressure, R the gas-constant, and subscripts 0 express the values at the ground surface. (H1-1-7) can be obtained by the following relation for a non-Boussinesq atmosphere with constant stability:

$$\bar{\theta}=\theta_0 e^{Sz}. \qquad \text{(H1-1-8)}$$

In computing the analytic solution, an isolated 3-D mountain with circular contours

$$Z_s(x,y)=\frac{h_m}{\left\{1+\left(\frac{x}{a}\right)^2+\left(\frac{y}{a}\right)^2\right\}^{\frac{3}{2}}}, \qquad \text{(H1-1-9)}$$

is employed according to Smith (1980) and Saito *et al.* (1998). The mountaintop height is set to $h_m=100$ m, and its shape is discretized on a grid mesh with $\Delta x=\Delta y=a/3$. The mesh size (Nx, Ny)=(128, 128) is used for the hydrostatic case, while the domain size for the x-direction is enlarged to (Nx, Ny)=(256, 128) for nonhydrostatic case because, in a nonhydrostatic case, the mountain wave extends leeward and the analytic solution is contaminated due to the periodic nature of the Fourier transform if the domain size is not sufficient. For the environmental atmospheric state, $U=8$ ms^{-1} and $N=0.01$ s^{-1} are chosen as in Saito *et al.* (1998).

H-1-2 Comparison between numerical and analytic solutions

Numerical solutions by the two models are computed with the following conditions:

1) Horizontal grid interval $\Delta x=\Delta y=a/3$, and model domain (Nx, Ny)=(62, 42).

2) 32 vertical levels with stretched grid interval $\Delta z=40$ m to 1200 m.

3) Rayleigh damping layers are imposed on the upper five levels.

4) Constant temperature/potential temperature lapse rate $d\theta/dz=3.0$ K/km is given. This lapse rate corresponds to the atmospheric stability $N=0.01$ s^{-1}.

a. Almost hydrostatic case

First, we show the result for the case of $\Delta x=2$ km. In this case, the horizontal scale of the mountain is $a=6$ km, and the product of the Scorer number N/U and a is 7.5, which means the horizontal scale of the mountain is much larger than the horizontal wave length of the buoyancy oscillation, and the nonhydrostatic effect is small. Figure H1-2-1 shows the vertical wind w obtained by the nonhydrostatic analytic solution (a and b), and the numerical model (c and d). In these figures, each scale on the horizontal axis represents the horizontal grid, and the mountaintop is located at $x=y=21.5$. The scale of the vertical axes of Figs. a and c is 400 m. As shown in these figures, the model simulates the characteristics of the analytic solution of the mountain wave well. The amplitude of simulated mountain waves is smaller than that of the analytic solution in upper layers. This underestimation of mountain waves near the upper boundaries is primarily attributed to the Rayleigh damping layer imposed near the model top (above $z=12$ km). Compared with Fig. C-1-3c of Ikawa and Saito (1991), the model solution is modified significantly in terms of the amplitude in the upper layers.

Another reason for the underestimation in the model solution may be the finite difference approximation.

Figure H1-2-2 shows the model solution when the horizontal advection terms are computed using the optional fourth-order accuracy scheme instead of the original second-order scheme. The simulated mountain wave is stronger in upper layers compared with Figs. H1-2-1c and d, and approaches the analytic solution more closely.

b. Nonhydrostatic case

Next, we show the results for $\Delta x = 0.4$ km. In this case, the horizontal scale a is 1.2 km. The product of the Scorer number and a is 1.5, which means that the nonhydrostatic effect is significant. Figure H1-2-3 shows vertical wind w obtained by the nonhydrostatic analytic solution, and the numerical model. Again, the numerical model simulates the characteristics of the analytic solution of the nonhydrostatic mountain wave very well. The radiation condition of the model works successfully, and the mountain wave propagates leeward through the right-side lateral boundary. Compared with Fig. C-1-3f of Ikawa and Saito (1991), the progress of the nonhydrostatic model is obvious.

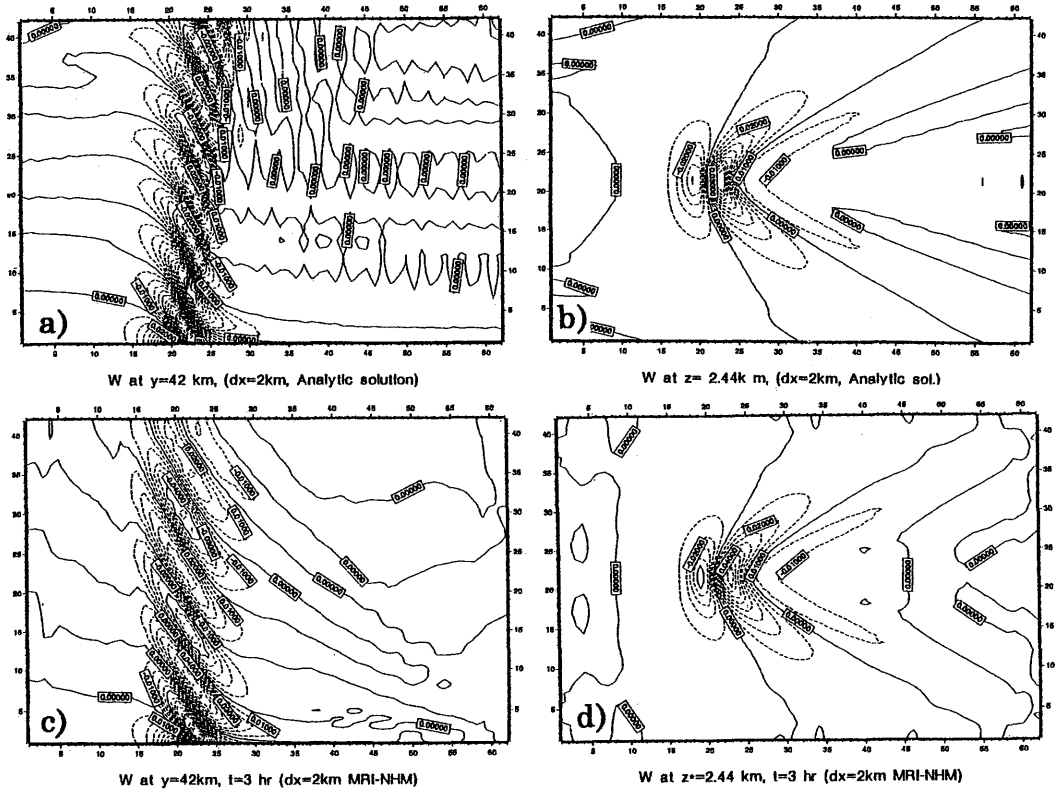

Fig. H1-2-1 3-D mountain waves by the nonhydrostatic analytic solution and model for $a = 6$ km ($\Delta x = 2$ km). a) Vertical cross-section of w through the mountaintop by the analytic solution. The contour interval is 1 cm s^{-1}. The graduations on the vertical and horizontal axes correspond to 400 m and 2 km, respectively. b) Horizontal cross-section of w at $z = 2.44$ km by the analytic solution. The graduations on the x- and y- axes correspond to 2 km. c) Same as in a), but by the numerical model at $t = 3$ h. d) Same as in b), but by the model at $t = 3$ h.

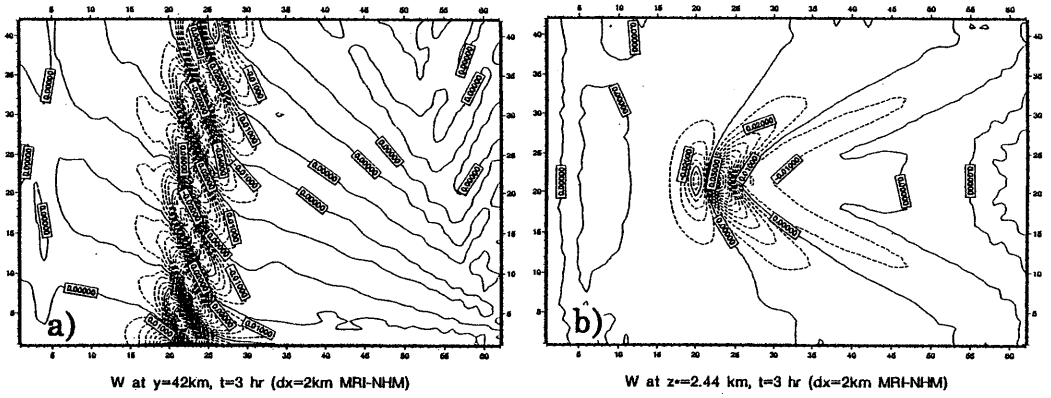

Fig. H1-2-2 Same as in Figs. H1-2-1 b) and d) but the fourth-order advection scheme is used.

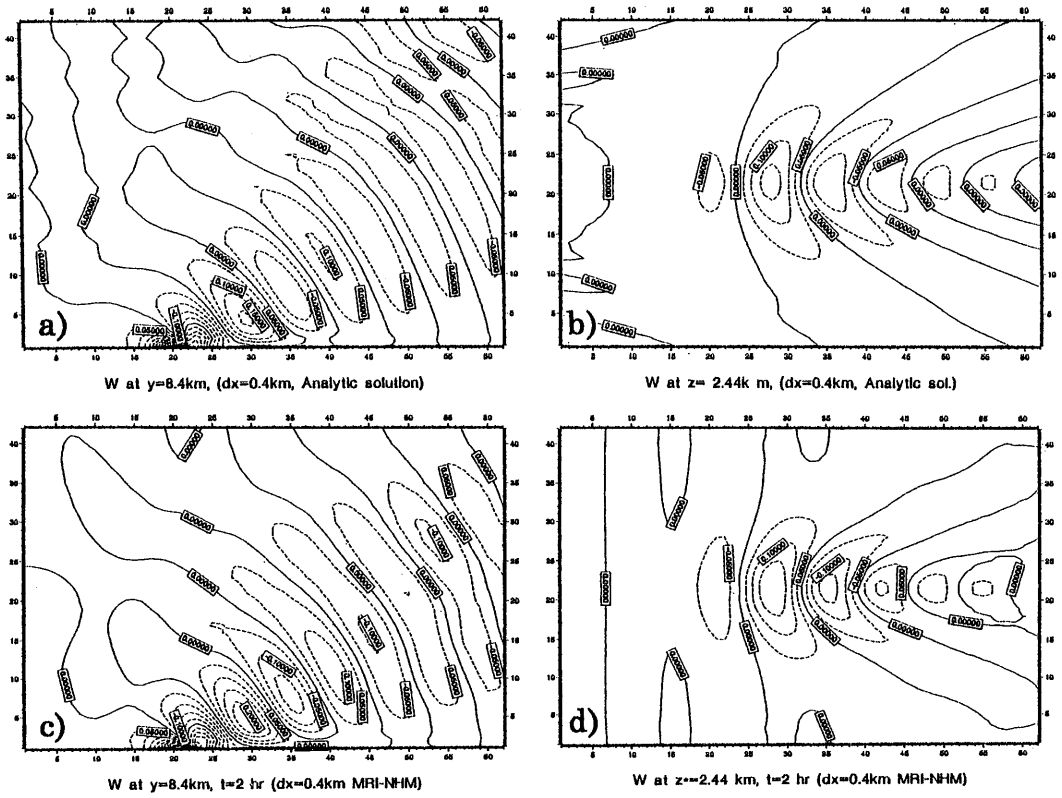

Fig. H1-2-3 Same as in Fig. H1-2-1 but for $a=1.2$ km ($\Delta x=0.4$ km). The contour interval is 5 cm s^{-1}. The scales on the x- and y- axes correspond to 0.4 km. Numerical model solutions are for the results at $t=2$ h.

H-2. Forecast experiment of the 1993 Kagoshima torrential rain[1]

H-2-1 Observation

Next we demonstrate the performance of the nonhydrostatic model as a regional forecast model. The event is the heavy rain that occurred in southern Kyushu, western Japan, in 1993. Figure H2-1-1 shows the surface weather map at 0900 JST 6 August. A stationary front runs from a depression around the east coast of China to south of Japan through Kyushu. Figure H2-1-2 shows the hourly rainfall analyses from 1600 JST to 2000 JST. An intense rainfall area corresponding to the mesoscale convective system moved east-southeastward, slowly passing over the southwestern part of Kyushu. Heavy rain exceeding 90 mm/hour was observed around Kagoshima City. The most intense period of the rainfall was from 1700 JST to 1900 JST. As seen in Fig. H2-1-3, a cyclonic circulation was analyzed in the observational surface wind pattern.

H-2-2 Forecast with 25 km horizontal resolution

First, we show the result of the forecast experiment with 25 km horizontal resolution (25 km-NHM). The model is nested with the Japan Spectral Model (JSM), an operational hydrostatic model of JMA. The nonhydrostatic model contains 82×82 grid points horizontally, which covers a domain of $(2000\ \mathrm{km})^2$ shown by a square in Fig. H-2-1. Vertically, 32-levels with variable grid intervals of $\Delta z = 40$ to 1160 m are employed. The time step is 30 s. Convective adjustment parameterization (Kato and Saito, 1995) is used jointly with warm-rain explicit cloud microphysics.

Figure H2-2-1 shows the sea-level pressure field at 1800 JST and three-hour precipitation from 1500 JST to 1800 JST forecasted by JSM and the nonhydrostatic model. Both models predict heavy rainfall in the southern part of Kyushu Island. As a whole, the nonhydrostatic model reproduces the forecast of JSM well. The mean surface pressure of the nonhydrostatic model decreases about 3.2 hPa from 0900 JST to 2400 JST, as shown in Fig. H2-2-2. This decrease of mean pressure corresponds to JSM's counterpart in the same domain. If we use the anelastic model, the decrease of the mean pressure for the 15 hours was only 0.6 hPa. The anelastic model cannot express the variation of mean surface pressure correctly because it assumes the preservation of total mass in the entire model domain.

H-2-3 Forecast with 5 km horizontal resolution

Forecast experiments were conducted with 10 km and 5 km horizontal resolutions. Here, we show the result of the 5 km simulation (5 km-NHM). The model domain consists of 122×122 grid points, which covers $(600\ \mathrm{km})^2$ around Kyushu. The vertical grid structure is the same as in 25 km-NHM. The initial and boundary conditions are supplied from JSM, while the initial time of the nonhydrostatic model is 1500 JST. As for cloud microphysics, a warm rain explicit scheme is used. The time step is 15 s, and the simulation is conducted up to 1440 Δt (6 hours).

Figure H2-3-1 shows the hourly rainfall predicted by 5 km-NHM, which corresponds to Fig. H-2-2. The maximum rainfall of each hour is 60 mm to 80 mm, and the correspondence between the observation and simulation is generally good except in north-south deviation (about 20 km) in the location of rainfall areas.

Figure H2-3-2a shows the horizontal wind at the lowest level of 5 km-NHM at 1800 JST. A cyclonic

[1]Part of this section was extracted from the results reported in Saito *et al.* (1998).

circulation appears northwest of the intense rainfall area. As seen in Fig. H2-3-2b, this circulation is a mesoscale depression with a circular contour of 1001 hPa. This mesoscale cyclone corresponds to Fig. H2-1-3 ; it is not seen in the initial condition and is predicted by neither JSM nor 25 km-NHM.

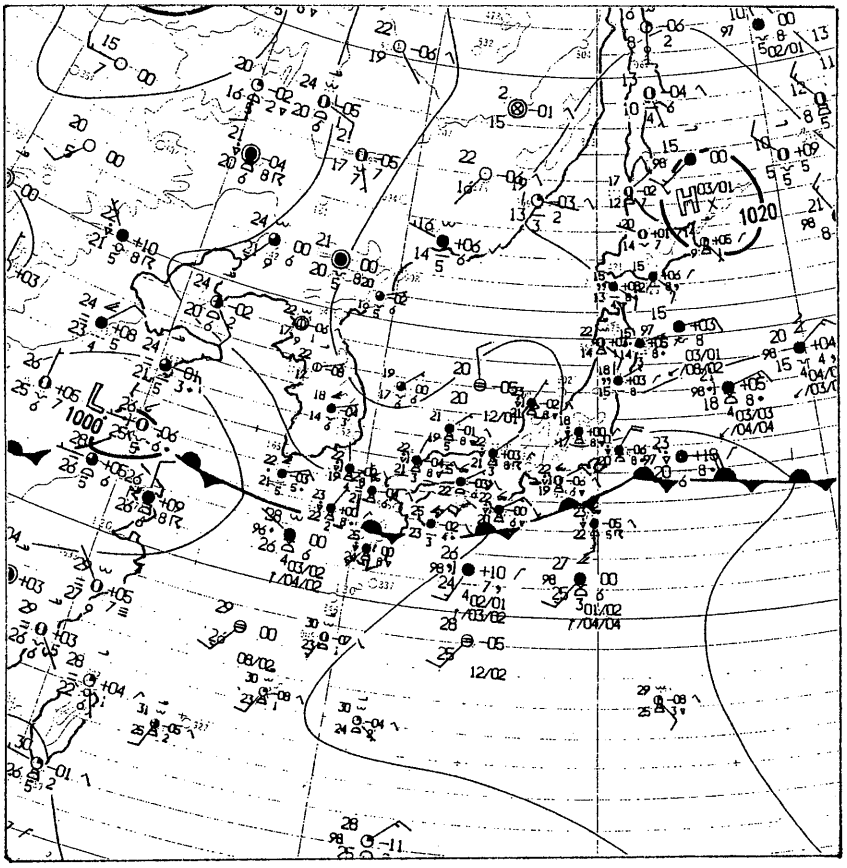

Fig. H2-1-1 Surface weather map at 0900 JST 6 August 1993. Contour interval is 4 hPa. After Saito (1997).

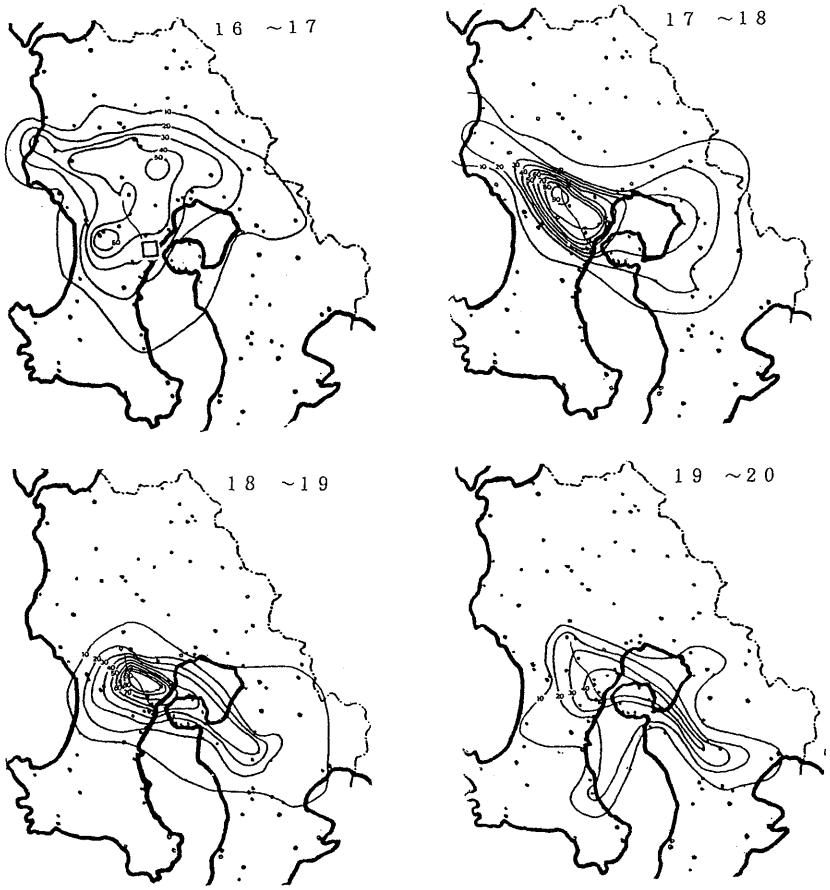

Fig. H2-1-2 Hourly rainfall from 1600 JST to 2000 JST, adopted from Sakurai and Hosoyamada (1994). Numbers in the upper right corner of each section show the local time (JST). Contour interval is 10 mm. Small square in the upper-left panel shows the location of Kagoshima City.

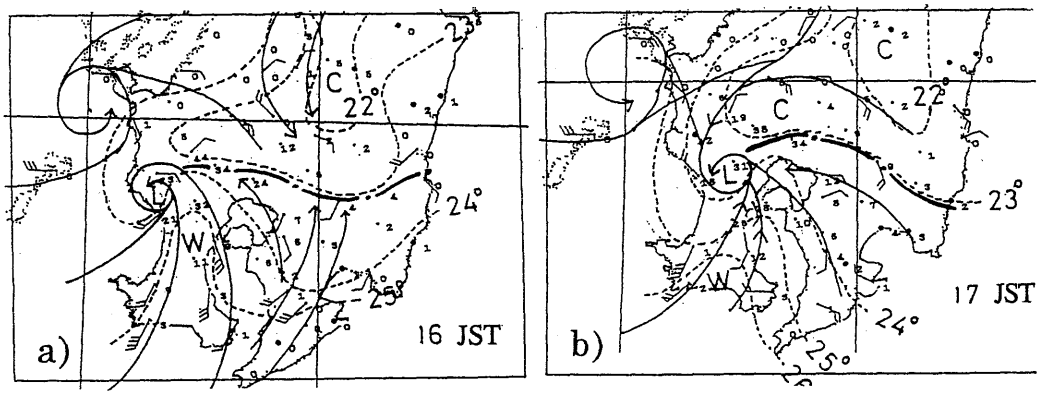

Fig. H2-1-3 Mesoscale analyses of local surface circulation adopted from Izumi (1994). The full barb and pennant indicate 1 knot and 5 knots, respectively.

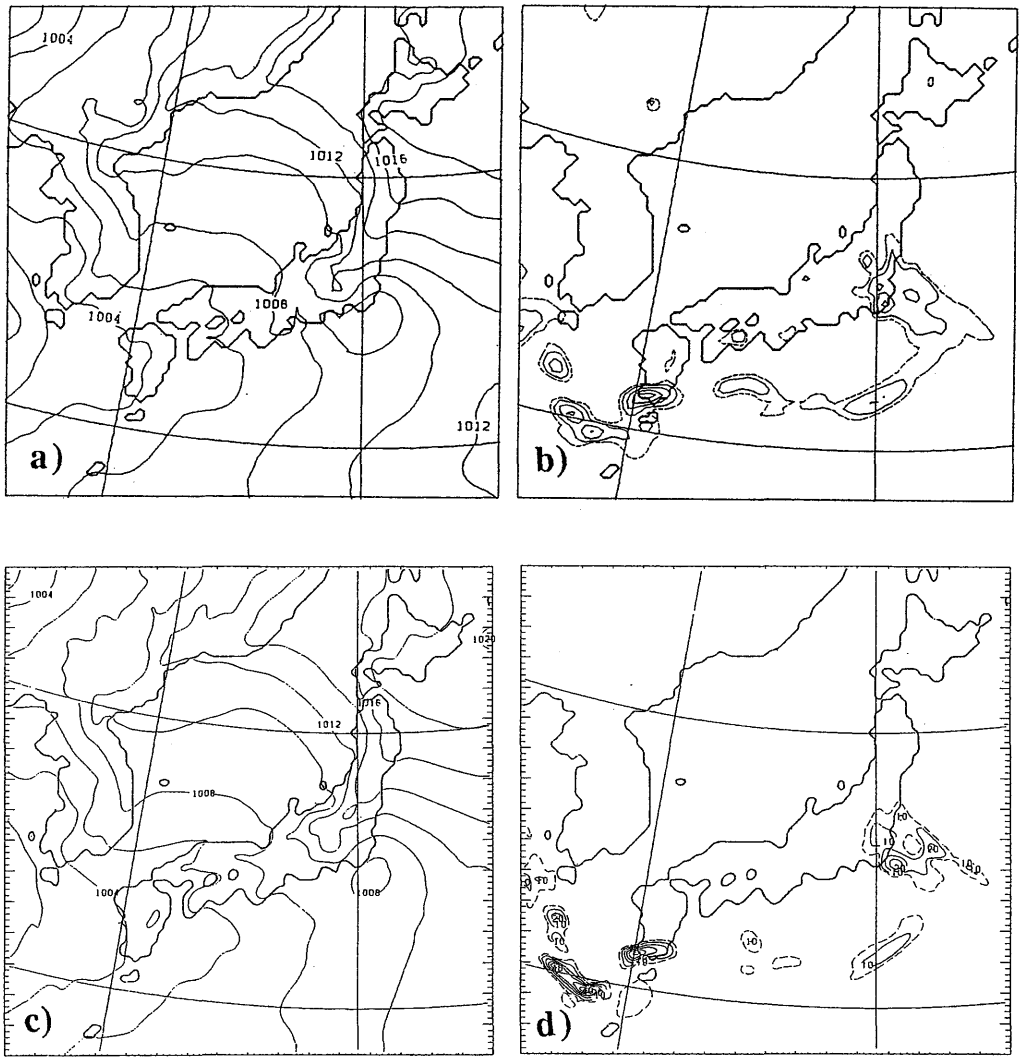

Fig. H2-2-1 **a)** Sea-level pressure field by JSM at 1800 JST. Contour interval is 2 hPa. **b)** Three-hour rainfall from 1500 JST to 1800 JST by JSM. Contour interval is 10 mm, while broken lines indicate 5 mm. **c)** Same as in a) but by the model. **d)** Same as in b) but by the model.

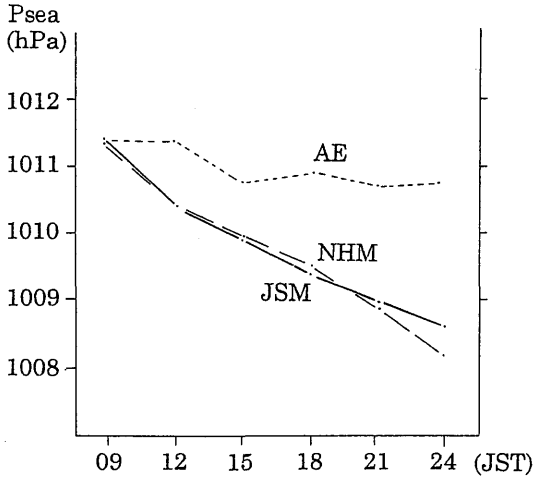

Fig. H2-2-2 Time sequence of mean sea-level pressure by JSM (solid line), 25 km-NHM (broken line) and AE-NHM (dotted line). The pressure is averaged over the domain of 25 km-NHM.

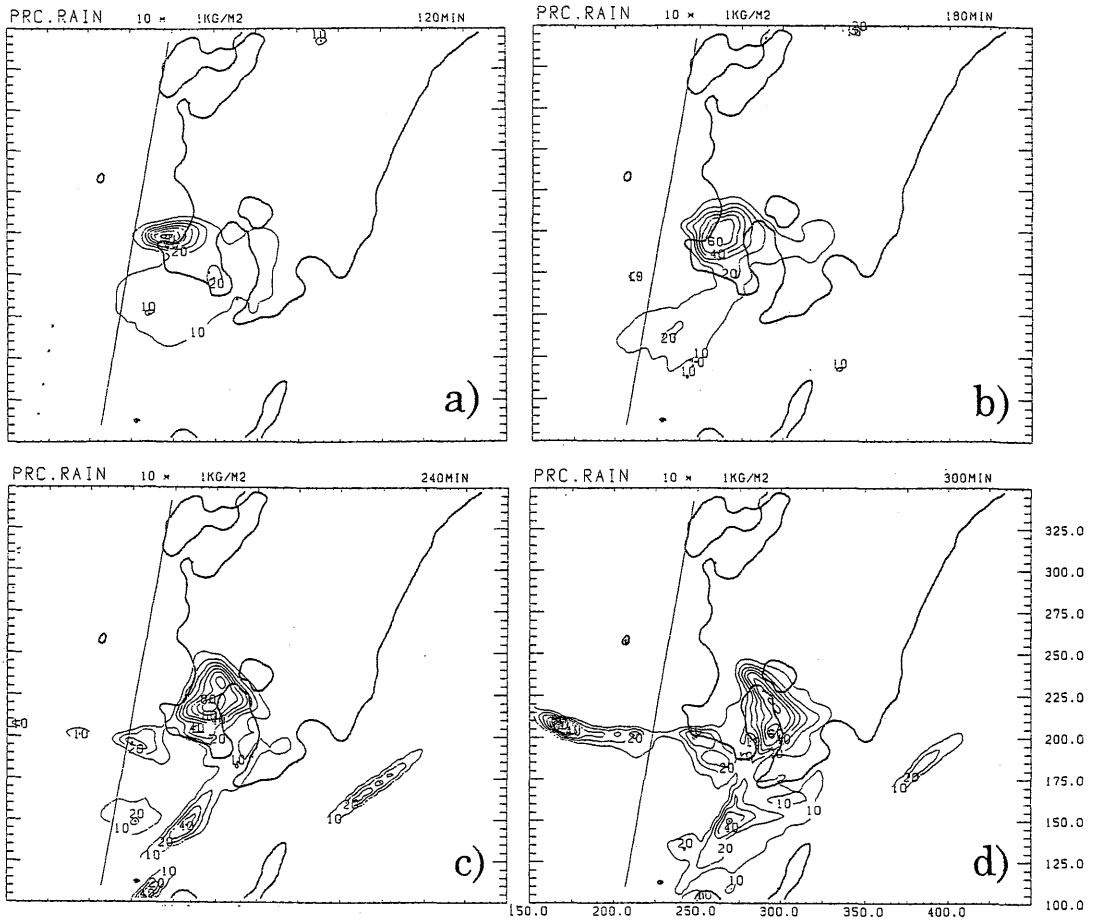

Fig. H2-3-1 Hourly rainfall by 5 km-NHM. Contour interval is 10 mm. **a)** 1600 JST to 1700 JST. **b)** 1700 JST to 1800 JST. **c)** 1800 JST to 1900 JST. **d)** 1900 JST to 2000 JST.

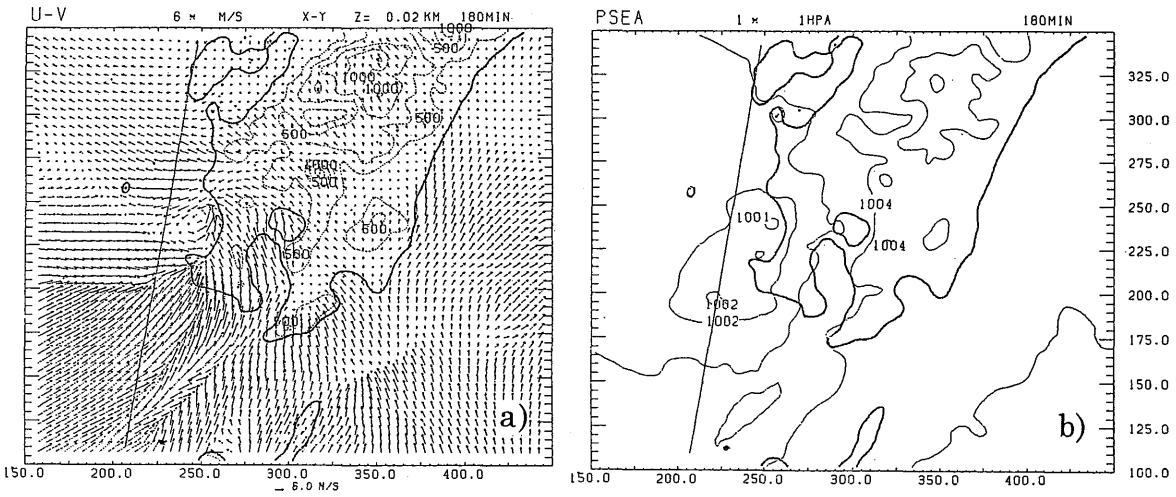

Fig. H2-3-2 **a)** Surface wind field of 5 km-NHM at 1800 JST. The lower center arrow indicates the scale of 6 m/s. **b)** Sea-level pressure field at 1800 JST. Contour interval is 2 hPa.

H-3. Statistical verification of rainfall prediction

H-3-1 Background and design of verification

The rainfall predicted by the MRI-NHM with a 10-km grid (NHM10) was verified during the 1996 Baiu season. The verification was compared with the results of RSM. These results were reported by Kato *et al.* (1988) and Saito and Kato (1999) in detail. This comparison is thought to have been conducted to examine the nonhydrostatic effect, because the RSM is a hydrostatic model. However, there are many differences between the model specifications of MRI-NHM and RSM, in addition to their dynamic frameworks. The most notable difference is found in the precipitation scheme employed in each model. Either the warm rain scheme that explicitly predicts the mixing ratios of cloud water and rainwater or the cold rain scheme that predicts those of cloud ice, snow and graupel in addition is employed in NHM10. In contrast, two parameterized convective schemes (*e.g.*, the Arakawa-Schubert and moist convective adjustment schemes) are used in conjunction with large-scale condensation in the RSM. A detailed comparison between hydrostatic and nonhydrostatic simulations of the development of moist convection has been conducted by Kato and Saito (1995).

Kurihara and Kato (1997) demonstrated that a clear diurnal variation of precipitation amount and intensity appeared in Kyushu during the 1996 Baiu season. They indicated that this variation comes from the effect of atmospheric radiation. The clouds suppressed the development of convections during the day and increased the convective instability at night. The effect of atmospheric radiation was also examined by excluding the atmospheric radiation process from NHM10. The atmospheric radiation is calculated by using the relative humidity (see G5-1-1).

Through use of the RSM with a resolution of about 20 km (operational RSM), the JMA provides a 51-hour weather forecast for the region in Fig. H3-1-1a twice a day. The RSM model specifications are summarized in Table 2 in Kato *et al.* (1998). The domain of RSM (RSM20) used in the present study covers about a quarter that of the operational RSM. Furthermore, the 10 km-resolution version of RSM (RSM10) is used to examine the influence of horizontal resolution. The domain of each model shown in Fig. H3-1-1a has $129 \times 129 \times 36$ grid points (the operational one is $257 \times 217 \times 36$). The orography of RSM20 is almost the same as that shown in Fig. H3-1-1a, and that of RSM10 is shown in Fig. H3-1-1b. The initial data of RSM10 and RSM20 (RSMs) are provided by the regional analysis, and the boundary conditions are provided by the output of the Global Spectral Model (GSM).

The horizontal domain for the MRI-NHM has 122×122 grid points while the vertical grid contains 38 levels with variable grid intervals of 40 m (near the surface) to 1120 m (at the top of the domain). The model top is located at 19.82 km. Each z-level almost corresponds to the σ-level in the RSMs. The domain is shown by the dashed square box in Fig. H3-1-1 ; the orography is almost the same as that of RSM10 (Fig. H3-1-1b).

Figure H3-1-2 shows the nesting procedure between GSM and RSM20 (RSM10) and between RSM20 and NHM10. The RSMs are one-way nested within the GSM forecast, and the integration time is 24 hours. The NHM10 is one-way nested within the RSM20 forecast, the initial time of which is 0000 UTC or 1200 UTC. The six-hour forecast of RSM20 (valid at 0600 UTC or 1800 UTC) is used for the initial data of NHM10. The integration time is 18 hours.

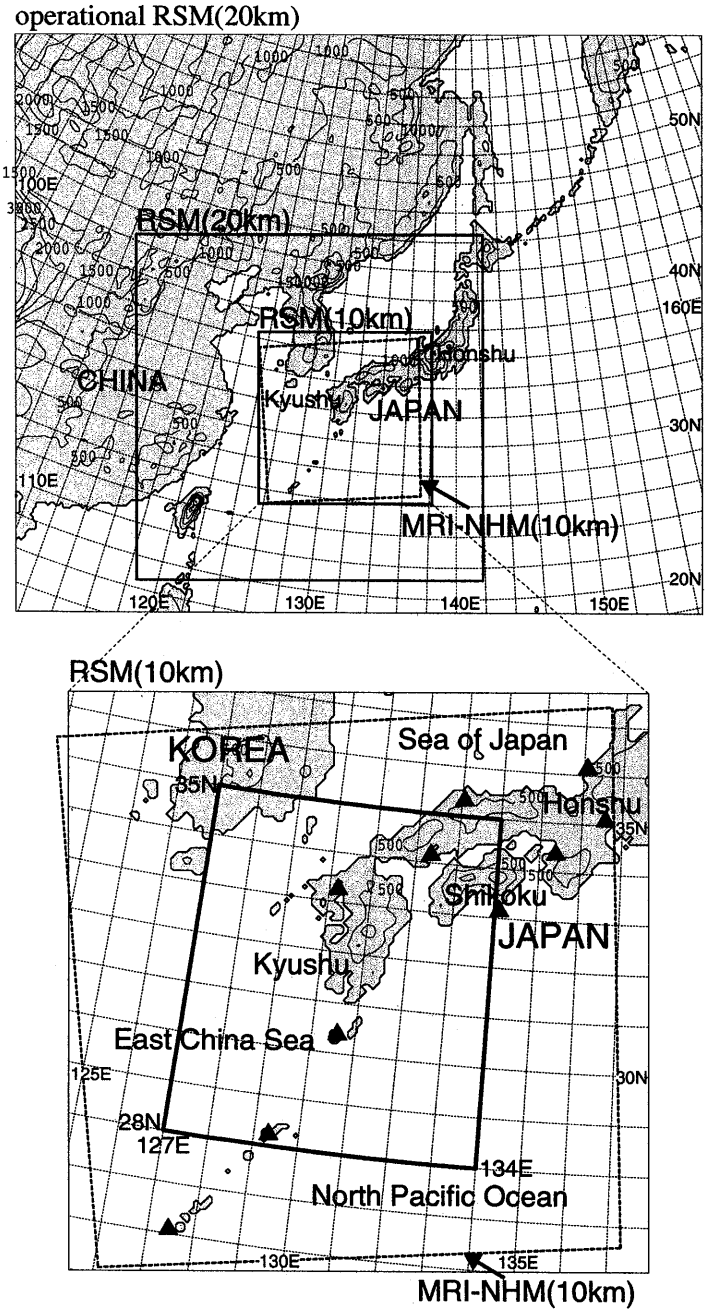

Fig. H3-1-1 (a) Domain and orography of the operational RSM. The domains of RSM10 and RSM20 are also shown by the small and large solid square boxes, respectively. The dashed square box represents the domain of NHM10. The orography of RSM20 is almost the same as that of the operational RSM. (b) Domain and orography of RSM10. The verification regionis endosed by thick colid lines (i.e., 28°N, 35°N, 127°E and 132°E). The solid triangle denotes the location of the JMA radars (from Kato *et al.*, 1998).

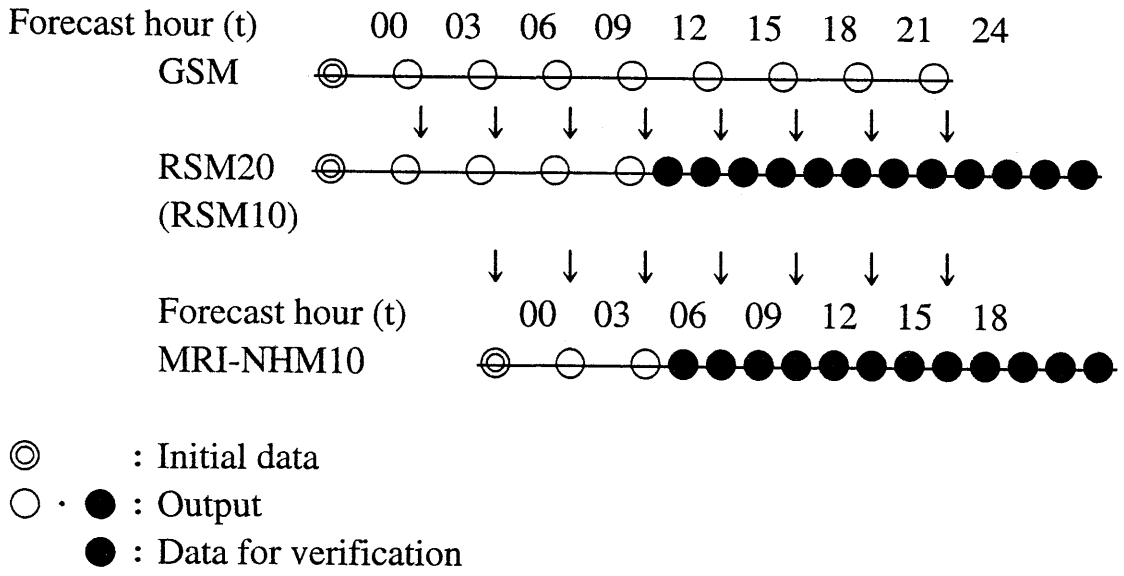

Fig. H3-1-2 Nesting procedure between numerical models

H-3-2 Verification method

The hourly accumulated rainfall simulated by NHM10 from the forecast time of 7 hours to 18 hours (FT= 7 to 18), and those by RSM10 and RSM20 from FT=13 to 24 (Fig. H3-1-2) are verified using Radar-AMeDAS analyzed rainfall (R-AR). The R-AR is a composite of the radar estimated fields, calibrated by AMeDAS raingauge data, for hourly-accumulated precipitation. The R-AR is obtained not only on land but also on the sea. The region of the verification is shown in the area surrounded by the thick solid lines in Fig. H3-1-1b (*i.e.*, the lines of 28°N, 35°N, 127°E, and 132°E). This region is almost covered by the operational radars of JMA (whose positions are denoted by the solid triangles in Fig. H3-1-1b). The period of verification is between the valid times of 0100 UTC, 20 June and 1200 UTC, 10 July.

The statistical accuracy is calculated as follows. Hourly accumulated rainfall is divided into grids of 0.5 degree (~50×50 km^2), whose horizontal size is almost equal to the smallest resolved scale of the phenomena by 10 km-resolution models. Figure H3-2-1 shows the conditions of hits, passes, and false alarms of predicted rainfall to R-AR. The rainfall in the neighboring grids and at earlier and later hours is included in each condition to allow for slight differences in the space and time between the prediction and analysis. The following statistical measures of accuracy were calculated in the region near Kyushu Island by counting the number of hits, passes, and false alarms.

$$\text{Threat score}=\frac{N_{hit}}{N_{hit}+N_{pass}+N_{false}}, \quad \text{(H3-2-1)}$$

$$\text{Bias score}=\frac{N_{hit}+N_{false}}{N_{hit}+N_{pass}}, \quad \text{(H3-2-2)}$$

$$\text{Hit rate}=\frac{N_{hit}}{N_{hit}+N_{pass}}, \quad \text{(H3-2-3)}$$

and

$$\text{False rate}=\frac{N_{false}}{N_{hit}+N_{pass}}, \quad \text{(H3-2-4)}$$

where N_{hit}, N_{pass}, and N_{false} are the numbers of hits, passes, and false alarms. The threat score is the statistical measure of accuracy taking into account the numbers of passes and false alarms; the prediction accuracy improves as the threat score comes closer to 1. The bias score represents the rate of the numbers of predicted times to observed times, *i.e.*, the prediction overestimates for bias scores >1 and underestimates for bias scores <1. The hit and false rates represent the rates of the numbers of hits and false alarms to the observed times.

H-3-3 Verification results

Table H3-3-1 presents the average of the total hourly-accumulated rainfall. The total rainfall predicted by all models tends to be overestimated in comparison with the R-AR. The RSM in particular has overestimated it by close to 50%; the RSM has a tendency to predict precipitation greater than the observation, even considering that the R-AR tends to be underestimated on the sea where no AMeDAS station exists (Forecast Division/JMA, 1995). This overestimation could be a result of a weak precipitation area, since a precipitation area over 1 mm h^{-1} has been predicted almost twice by the RSM (not shown). In contrast, the NHM10 predicted smaller areas for weak precipitation and larger areas for heavy precipitation than the RSM, due to the explicit treatment of convection without any convection-parameterization scheme. The overestimation of heavy rainfall is greater in the results with a warm rain scheme than those with a cold rain scheme. The effect of an ice phase could suppress the excess development of convections.

Atmospheric radiation hardly affects the heavy precipitation and total rainfall, while its effect appears clearly in the diurnal variation of precipitation (Fig. H3-3-1). The peak of precipitation has a time lag with the NHM10 without an atmospheric radiation scheme, because it takes several hours for the influence of the boundary condition supplied by the RSM to spread to the center of the model domain. The diurnal variation of precipitation agrees well with the R-AR for the NHM10 with an atmospheric radiation scheme.

Figure H3-3-2 shows the threat and bias scores and the hit and false rates of NHM10, RSM10, and RSM20. The results for the NHM10 are presented for cases with a warm rain scheme and without an atmospheric radiation scheme (NHM10(Warm)) and for those with both cold rain and atmospheric radiation schemes (NHM10(C+R)). The threat scores of NHM10 are slightly worse, but considerably better than those of RSM10.

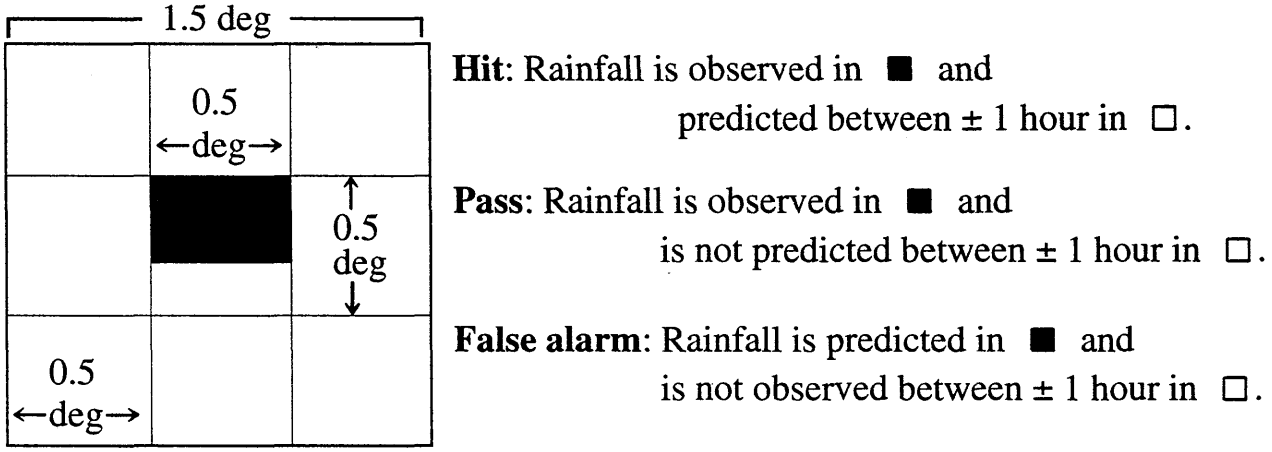

Fig. H3-2-1 Conditions of hits, passes, and false alarms of predicted rainfall for Radar-AMeDAS analyzed rainfall.

The NHM10(C+R) has good accuracy for weak precipitation in particular, close to that of RSM10. NHM10(C+R) has better bias scores than NHM10(Warm) over the whole precipitation intensity. However, the small bias scores of RSM (*e.g.*, 10 to 20 mm h^{-1}) indicate that the RSM can predict heavy rainfall to a small extent. The RSM10 has a high hit rate for weak precipitation, while the NHM10 has a relatively high hit rate for heavy precipitation. The NHM10 hits almost half the numbers for precipitation of 10 to 20 mm h^{-1}. In the results of both NHM10 and RSM10, the precipitation intensity with a relatively high false rate has also a relatively high hit rate (*e.g.*, 1 to 2 mm h^{-1} for the RSM10, and 20 mm h^{-1} for the NHM10). Therefore, a good threat score is obtained when the precipitation intensity is overestimated.

Although a 10-km grid cannot resolve individual convective cells, the NHM10 with an explicit precipitation scheme improved the prediction of heavy rainfall compared to the RSM10. This could be because explicit treatment of cloud-scale processes strongly influences the formation of heavy rainfall during the Baiu season. This improvement indicates that the NHM10 with an explicit precipitation scheme has good accuracy for a numerical weather prediction model, even when any convection-parameterized scheme is used conjunctionally. However, a new precipitation scheme suitable for a 5 to 10 km model must be developed to improve the prediction of weak precipitation and suppress the overestimation of heavy precipitation.

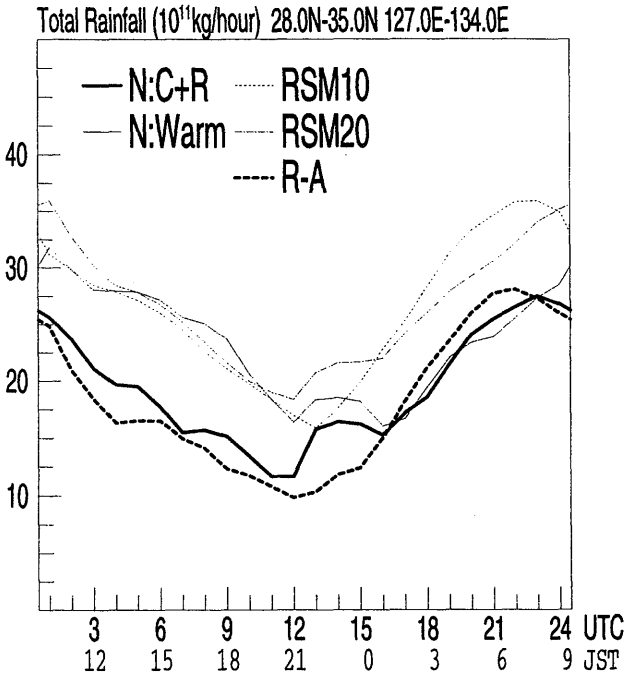

Fig. H3-3-1 Diurnal variation of the total rainfall. The thick solid line indicates the variation of NHM10 with an atmospheric radiation scheme, the thick dashed line represents that of NHM10 without an atmospheric radiation scheme, the thin solid line indicates that of RSM10, the dash-dotted line that of RSM20, and the thick dashed line that of R-AR (from Saito and Kato, 1999).

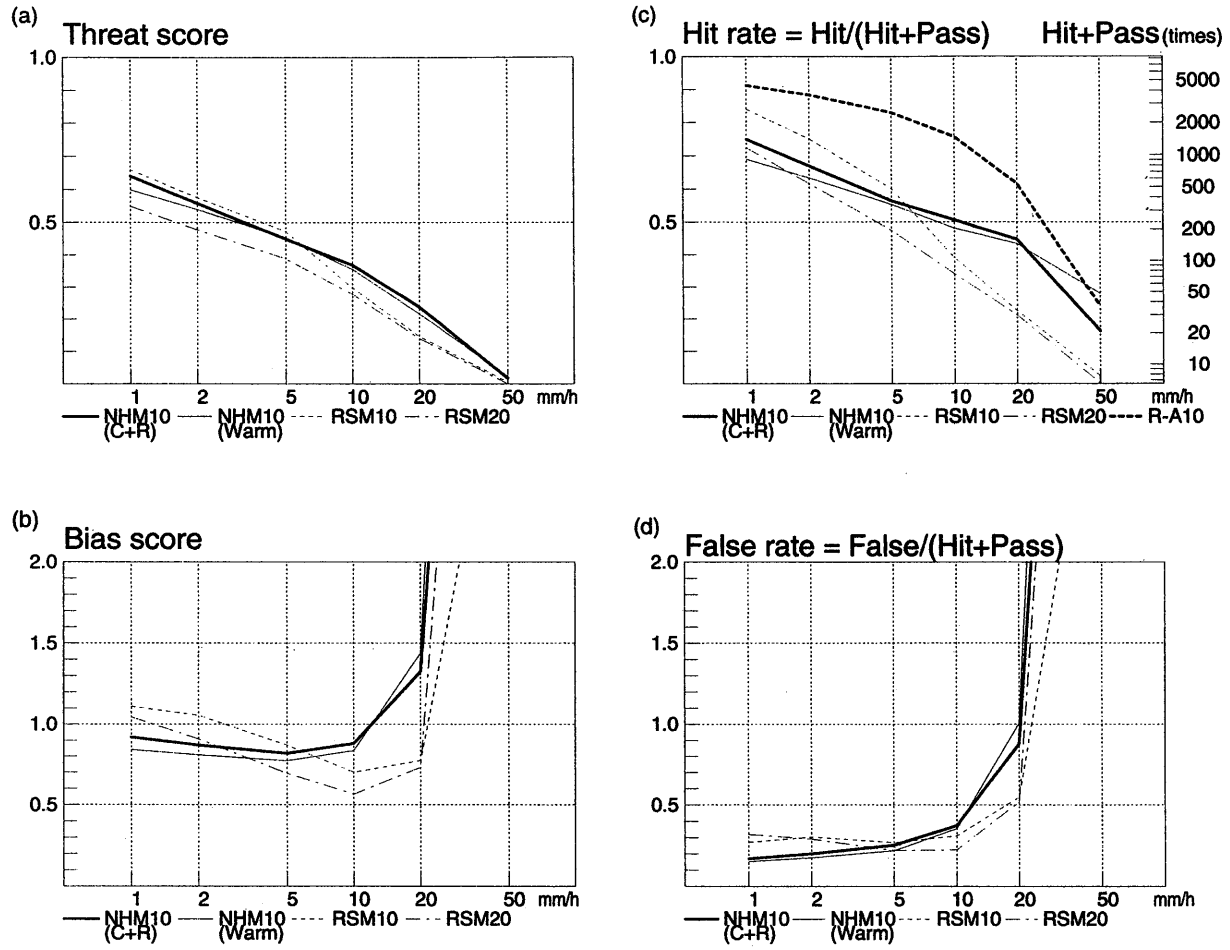

Fig. H3-3-2 Statistical scores of NHM10 with an atmospheric radiation scheme (thick solid line), NHM10 without an atmospheric radiation scheme (thin solid line), RSM10 (thin dashed line), and RSM20 (thin dash-dotted line). The abscissa denotes the hourly-accumulated rainfall. (a) Threat score. (b) Bias score. (c) Hit rate. (d) False rate. The numbers of observed times for R-A10 are shown by the thick dashed lines in (c) (from Saito and Kato, 1999).

Table H3-3-1 Average of total precipitation and precipitation area

	Total Rainfall [10^{11} kg h^{-1}]	Area of Rainfall [100 km^2] >20 mm	>10 mm	>5 mm	>1 mm
NHM10 (C+R)	19.01	17.66	46.88	93.6	175.7
NHM10 (Warm)	22.99	26.53	56.64	102.9	272.7
RSM10	26.03	8.41	37.65	115.5	595.6
RSM20	26.05	5.45	36.53	118.7	612.7
R-A10	17.75	8.82	42.85	112.3	385.4
R-A20	17.75	6.20	35.84	100.7	332.8

H-4. Cloud resolving simulation－winter marine stratocumulus

In winter, a continental cold air mass sometimes flows out over a warmer sea, supplying a great amount of heat and water vapor. As a consequence of this air-mass transformation, a maritime mixed layer develops, and stratocumulus is generated in its upper layer. In the Japanese Cloud and Climate Study (JACCS), aircraft observations of cloud physics and radiation were performed for lower clouds around the Japanese Islands during FY1996 and FY1997 winter seasons. The FY1996 experiment was conducted for marine stratocumulus in the cloud streets west of Kyushu in January 1997. In this study, we tried to reproduce observed features of stratocumulus by using a 3-D non-hydrostatic model and investigated the heat balance in the mixed layer.

H-4-1 Outline of numerical experiment

The elastic version of MRI-NHM (Ikawa and Saito, 1991 ; Saito and Kato, 1996) with a horizontal grid size of 1km was used. The calculation domain has a $300\times300\times38$ horizontal and vertical grid. In this study, the cloud physics in the model contains the cold rain scheme, and the atmospheric radiation scheme for the cloud-resolving model (G-5-2) is used. The initial and boundary conditions for MRI-NHM are provided from the output produced by RSM. MRI-NHM is one-way nested within the RSM forecast with an initial time of 2100 JST, 21 January 1997.

H-4-2 Results

Figure H4-2-1 shows the horizontal map of the liquid water path (LWP) simulated by MRI-NHM at 0300 UTC on 22 January 1997 (nine-hour forecast). Several cloud streets are obtained and roughly correspond with satellite observations (Fig. H4-2-2). They are about 10km wide and extend north and south. Figure H4-2-3 presents the vertical profile of liquid water content (LWC) along the cloud street. Aircraft observations (Fig. H4 -2-3a) show that clouds contain LWC of about 0.7 gm^{-3} and extend from 1 to 2 km in height. The vertical distribution and the magnitude of LWC simulated by MRI-NHM are similar to observations (Fig. H-4-2-3b).

Figure H4-2-4 shows the vertical profiles of the components of heating rate averaged in the box in Fig. 1. The heating is seen in the whole layer. In the sub-cloud layer, the heating due to convergence of the upward sensible heat flux is greater than the cooling due to large-scale advection. In the under part of the cloud layer, the sum of the heating due to the convergence of the upward sensible heat flux, condensation and radiation is greater than the cooling due to large-scale advection. In the upper part of the cloud layer, the sum of the cooling due to the divergence of the upward sensible heat flux, evaporation and radiation is almost balanced by the heating due to large-scale advection. Above the cloud, the heating due to large-scale advection, especially subsidence, is dominant. Furthermore, the radiative heating and cooling is not small compared with other terms.

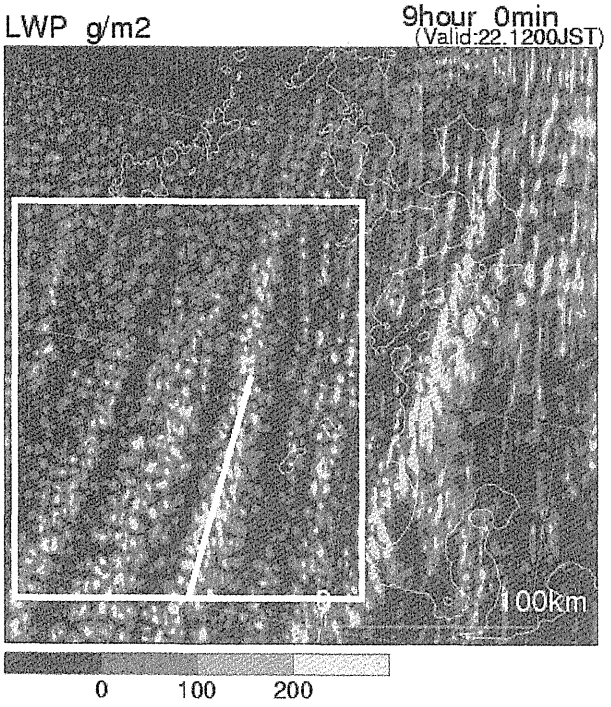

Fig. H4-2-1 Horizontal distribution of LWP at 0300 UTC on 22 January 1997 (nine-hour forecast). Solid line (box) is used in Fig. H-4-2-3 (Fig. H-4-2-4).

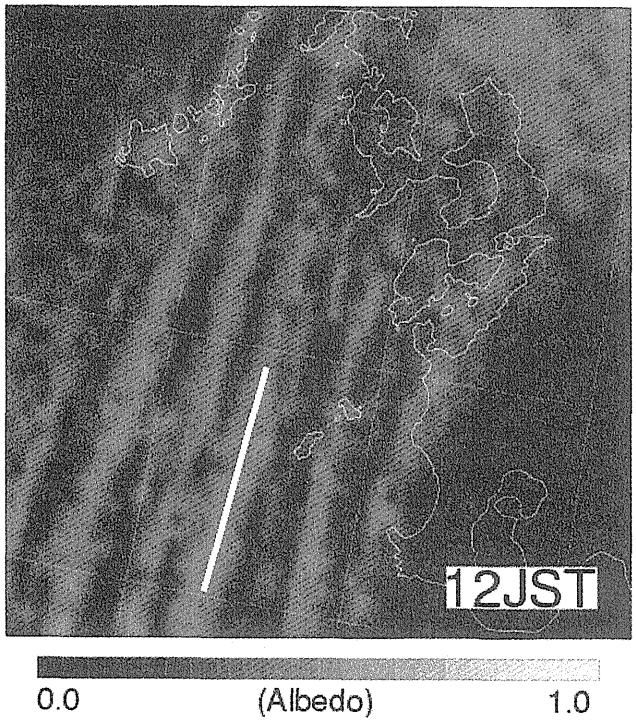

Fig. H4-2-2 Visible satellite image at 0300 UTC on 22 January 1997. Solid line denotes flight path of the aircraft.

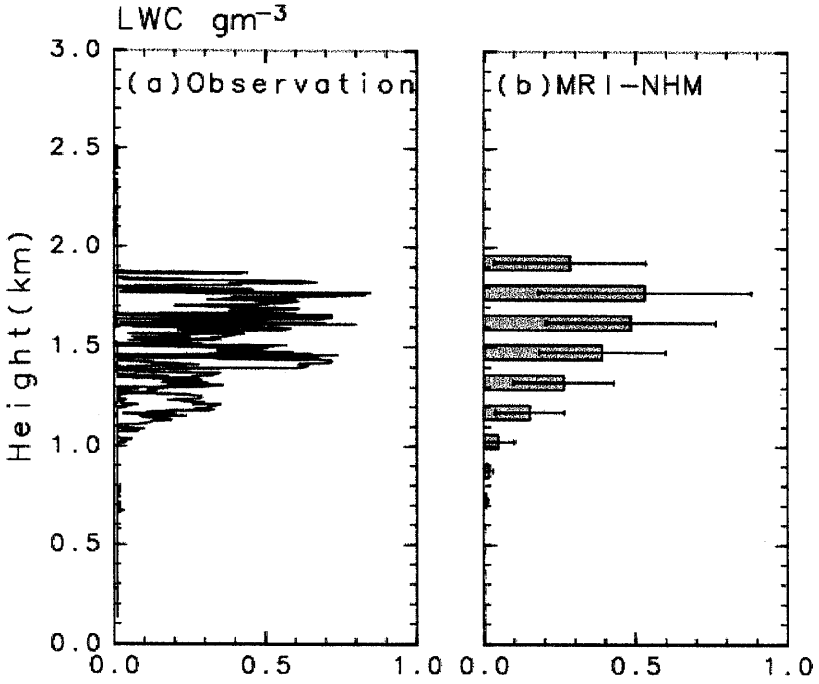

Fig. H4-2-3 Vertical profile of LWC of (a) aircraft observations along the solid line in Fig. H4-2-2 and (b) MRI-NHM simulation along the solid line in Fig. H4-2-1. Bar graphs (error bars) in (b) denote mean value (standard deviation).

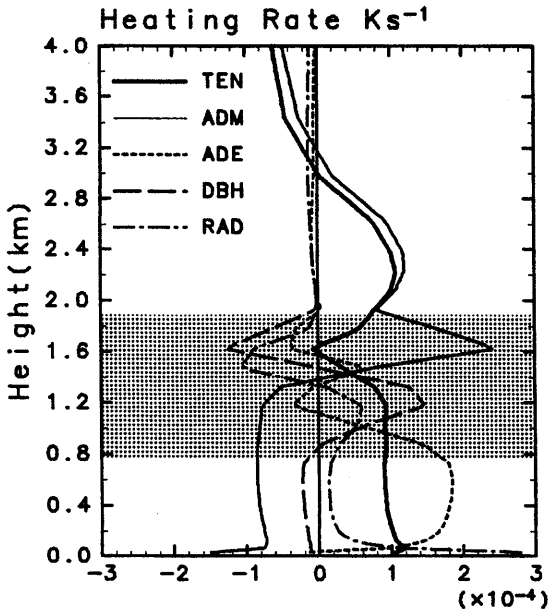

Fig. H4-2-4 Vertical profiles of heating rate components, averaged in solid box area in Fig.H-4-2-1, at 0300 UTC on 22 January 1997. Local time tendency is indicated by a thick solid line, area-scale advection by a thin solid line, convergence of the convective heat flux by a dotted line, the effect of condensation and evaporation by a dashed line, and the effect of radiation by a dash-dotted line. The hatched area denotes a cloud layer.